Optical diagnostics-based numerical modeling of a compression-ignition optical research engine implementing ducted fuel injection

Original
Optical diagnostics-based numerical modeling of a compression-ignition optical research engine implementing ducted fuel injection / Segatori, C.; Orlando, M.; Piano, A.; Millo, F.; Mueller, C. J.. - In: APPLICATIONS IN ENERGY AND COMBUSTION SCIENCE. - ISSN 2666-352X. - ELETTRONICO. - 24:(2025). [10.1016/j.jaecs.2025.100408]

Publisher:
Elsevier

Published
DOI:10.1016/j.jaecs.2025.100408

Applications in Energy and Combustion Science 24 (2025) 100408

Contents lists available at ScienceDirect

Applications in Energy and Combustion Science

journal homepage: www.sciencedirect.com/journal/applications-in-energy-and-combustion-science

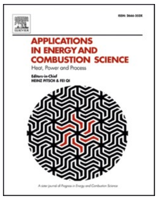

Optical diagnostics-based numerical modeling of a compression-ignition optical research engine implementing ducted fuel injection

C. Segatori [a], M. Orlando [a], A. Piano [a,*], F. Millo [a], C.J. Mueller [b]

[a] Politecnico di Torino, Italy
[b] Sandia National Laboratories, USA

ARTICLE INFO

Keywords:
Ducted fuel injection
Optical engine
Computational fluid dynamics
OH* chemiluminescence
Soot natural luminosity

ABSTRACT

Ducted fuel injection (DFI) is a promising strategy to dramatically reduce engine-out soot emissions from compression-ignition (CI) engines. To accelerate the integration of DFI into real-world engines, computational fluid dynamics (CFD) is a powerful tool for its understanding and optimization. Although CFD has been largely adopted for investigating DFI in CI engines, accuracy and reliability of the numerical outcomes remain often questionable.

Therefore, this article proposes a step forward in the CFD model development and validation process of a CI optical engine implementing DFI, considering both global and local perspectives. Indeed, leveraging the optical diagnostics dataset, the correct reproduction of the combustion and emissions formation processes – across a range of loads and oxygen levels for both CDC and DFI configurations – was tested not only in terms of typical aggregated values (i.e., pressure, burn rate, engine-out emissions) but also locally in terms of lift-off length, flame evolution, and soot natural luminosity (NL). For the latter a proper methodology was used to virtually replicate soot NL distribution starting from the CFD variables. Despite the complexity of this luminosity-based comparison, the model was found to reasonably replicate the main trends, for both CDC and DFI, thus highlighting predictive capability, not only in terms of engine-out soot emission values, but also of the in-cylinder soot formation/oxidation processes. Moreover, the present results demonstrate the robustness of the methodology to compute a virtual NL from CFD outputs, which could be of interest to thoroughly validate combustion models every time soot prediction accuracy plays an important role.

1. Introduction

Currently, compression-ignition (CI) engines based on the conventional diesel combustion (CDC) process are widely used for heavy-duty transport and local power generation [1]. Despite their massive utilization, CDC typically leads to relatively high levels of engine-out soot and nitrogen oxides (NOx) emissions, due to the local mixture conditions in the autoignition zone and the high-temperature diffusive flame, typically abated through complex and expensive aftertreatment systems [2,3]. To address this problem, the so-called leaner-lifted flame combustion (LLFC) is a CDC variant which aims to achieve soot-free combustion by maintaining equivalence ratios below 2 at the lift-off length (LOL). This could theoretically be achieved through one or more of the following actions: smaller-orifice injectors, higher injection pressures, high dilution levels, and oxygenated fuels. However, experimental studies demonstrated that LLFC is constrained to low-load conditions and configurations with a limited number of nozzle orifices due to adverse phenomena such as spray-to-spray interactions and the re-entrainment of combustion products [4]. Addressing these limitations has driven interest in solutions capable of enhancing air-fuel mixing before the LOL.

In this context, ducted fuel injection (DFI), a technology patented by Sandia National Laboratories [5], has emerged as a promising solution. DFI consists in injecting the fuel down the axis of a small duct positioned within the combustion chamber at a certain distance from the injector orifice exit, and its soot mitigation potential was demonstrated in several works. Experimental analyses in constant-volume vessels have demonstrated the capability of DFI technology to significantly reduce soot natural luminosity [6] and soot mass [7] across several operating conditions, varying ambient temperature, ambient density, and oxygen concentration. Moreover, these initial studies underlined that the soot mitigation mechanisms driven by duct adoption extend beyond the

---

* Corresponding author.
E-mail address: andrea.piano@polito.it (A. Piano).

https://doi.org/10.1016/j.jaecs.2025.100408
Received 11 July 2025; Received in revised form 26 September 2025; Accepted 3 October 2025

simple increase in LOL and necessarily include additional entrainment and/or mixing phenomena occurring upstream of it. These speculations were subsequently confirmed and explained by several numerical investigations which highlighted that, on the one hand, DFI enhances the gas entrainment upstream of the duct inlet due to the establishment of a low pressure region inside the duct, on the other hand, DFI enhances the turbulent mixing, both inside and downstream of the duct, with respect to the CDC configuration [8–15]. Finally, a recent experimental study employing optical diagnostics (i.e., Schlieren imaging, OH* chemiluminescence, and broadband luminosity to characterize the reacting flow; 2D laser absorption and scattering to quantify the non-reacting mixing fields) in a high-pressure vessel further elucidated DFI physics [16]. This work corroborated the abovementioned numerical findings regarding air entrainment and turbulent mixing, and it highlighted that the reduction in residence time for soot formation between the LOL and soot oxidation is another driver for DFI performance.

Apart from understanding, investigating the capability of DFI concept to effectively work and curtail soot when moved from the test vessel to the engine combustion chamber is crucial for the DFI technology success. Some research works studied the possibility to implement DFI in existing CI engines geometry via both experiments and simulations, highlighting that direct retrofit is not straightforward and a new combustion system design and calibration could be required. In particular, LOL shortening [17,18] (due to the re-entrainment of hot combustion products) and poor late-cycle soot oxidation [18–20] (due to lower temperatures of DFI system walls, lower available air for oxidation hidden by the DFI system volume, enhanced spray/bowl interaction, and late-cycle swirl level reduced by the flow-ducts interaction) could lead to higher engine-out soot emissions for DFI compared to CDC.

Therefore, while promising results have been achieved with DFI in test vessel experiments, it is still of paramount importance to investigate DFI under realistic engine conditions to provide essential information targeted at the successful implementation of this concept. Among the facilities supporting this kind of research, the Sandia Compression-Ignition Optical Research Engine (SCORE) has played a crucial role for the advancements in this field so far. This 1.72 L single-cylinder engine offers optical access to the combustion chamber through a fused-silica window integrated into a flat piston bowl with a vertical side, enabling in-depth visualization of DFI behavior in an engine environment. In Table 1 the experimental and numerical works about DFI performed on the SCORE case study are reported.

Focusing on the experimental studies reported in Table 1, they generally pointed out that DFI can maintain remarkable soot reduction benefits inside a CI engine working up to 22 bar gross indicated mean effective pressure (IMEPg), using a two-hole or four-hole injector of

Table 1
Published experimental and numerical investigations on DFI using the SCORE case study.

Investigators	Method	Injector N°holes x µm	IMEPg [bar]	Fuel	Highlights
Nilsen et al. [21]	EXP (In-cylinder pressure, exhaust emissions (gaseous and particle mass), and optical diagnostics)	2 × 110	2.6	CF_A	Proof-of-concept of DFI implementation in a CI engine combustion chamber
Nilsen et al. [22]	EXP (In-cylinder pressure, exhaust emissions (gaseous and particle mass), and optical diagnostics)	4 × 110	2.5÷ 8.7	CF_B	Demonstration of the DFI capability to break the soot/NOx trade-off with dilution and attenuate engine-out soot emissions under a wide range of operating conditions
Nilsen et al. [23]	EXP (In-cylinder pressure, exhaust emissions (gaseous and particle mass), and optical diagnostics)	4 × 110	1÷10	CF_B	Investigation of DFI at higher load conditions, highlighting the need for calibration for optimal DFI operation, due to late-cycle soot formation
Mueller et al. [24]	EXP (In-cylinder pressure, exhaust emissions (gaseous and particle mass), and optical diagnostics)	2 × 110	2.6	MD25, T25	Demonstration of synergies between DFI and oxygenated fuels in terms of soot formation reduction
Nilsen et al. [25]	EXP (In-cylinder pressure, exhaust emissions (gaseous, particle mass and particle number), and optical diagnostics)	4 × 110,175	6.8÷13.4	CF_B	Study on the impact of larger injector nozzle diameter (to enable higher load levels) on DFI performance and correlations with duct geometry variation
Wilmer et al. [26]	EXP (In-cylinder pressure and exhaust emissions (particle mass and number) diagnostics)	4 × 175	13.3	CF_B	Study on the impact of DFI on the particle number (PN) and the particle mass (PM) distributions, demonstrating that DFI produces both lower PN and lower PM for particulate matter >23 nm in size
Nyrenstedt et al. [27]	EXP (In-cylinder pressure, exhaust emissions (gaseous and particle mass), and optical diagnostics)	4 × 175	1÷10	CF_C, HEA00, HEA33, HEA67	Study on the coupling of DFI with low-lifecycle-CO_2 fuels to meet heavy-duty future on-road and off-road emissions regulations for California, aiming at undersizing the amount of aftertreatment
Sener et al. [28]	CFD (RANS)	4 × 110	6.8	Diesel #2	Study on the impact of DFI on heat transfer
Buurman et al. [29]	EXP (In-cylinder pressure, exhaust emissions (gaseous and particle mass), and optical diagnostics)	4 × 221	6÷22	R80B20	Demonstration of DFI capability to properly work up to full load conditions by using larger injector orifices, highlighting the potential need for combustion system adjustments for optimal performance
Yraguen et al. [30]	EXP (In-cylinder pressure, exhaust emissions (gaseous and particle mass), and optical diagnostics)	2,4 × 110	0.7÷8.7	CF_A, CF_B	Study on the impact of the number of ducts on the DFI performance and investigation to mitigate late-cycle soot production
Liu et al. [31]	CFD (RANS)	4–8 × 175	10	Diesel #2	Study on the impact of several engine parameters (swirl ratio, piston geometry, compression ratio, number of injector orifices, split injection strategy, and EGR) on DFI performance to define trends for DFI combustion systems optimization
Sener et al. [32]	CFD (RANS)	4 × 110	6.8	Diesel #2	Study on the impact of spray-duct horizontal, vertical, and rotational misalignments on DFI performance

various nozzle hole diameters. Moreover, these investigations highlighted that DFI could break the conventional soot/NOx trade-off with dilution, achieving simultaneous reductions in soot and NOx emissions thanks to high EGR rate, even meeting regulatory targets without aftertreatment systems under certain conditions [22,27]. In addition, some of these studies demonstrated the possibility to couple DFI with low-lifecycle-CO_2 fuels, as needed in a low-soot low-lifecycle-CO_2 scenario for heavy-duty CI engine-based transportation.

Focusing on the numerical side, computational fluid dynamics (CFD) can be a game changer in the DFI development process, by providing a deeper understanding of phenomena that experiments cannot readily measure and by boosting the amount of data generated as a virtual test rig. Particularly, considering the numerical works cited in Table 1, they have provided valuable contributions to understanding heat transfer [28], optimization strategies [31], and the influence of geometric tolerances [32]. Although the predictive capabilities of the used models were in line with the scope of these works, they were not proved when varying configuration — such as from CDC to DFI — and/or operating conditions, while keeping the numerical setup parameters constant. This approach does not ensure solution accuracy if these models are employed for fully predictive analyses, especially when hard-to-predict quantities (e.g., soot emissions) are of interest. Moreover, the validation methodology employed in these studies only relies on macroscopic variables such as in-cylinder pressure, burn rate, and engine-out emissions, while the local phenomena that are fundamental for CFD investigations are not addressed. For this purpose, validation against optical images is of paramount importance to ensure the reliability of CFD models in capturing spatially distributed phenomena, diving into flame structures and soot distributions, thus assessing model accuracy. In this context, a robust methodology to consistently compare CFD results with optical data is also crucial.

Therefore, this study aims at defining a high-fidelity 3D-CFD model for the SCORE under both CDC mode and DFI mode over multiple operating points, leveraging on the experimental dataset presented in [27] and the associated optical data related to OH* chemiluminescence and natural luminosity. In particular, the combustion and emissions formation processes were validated in terms of both aggregated values (i.e., pressure and burn-rate traces, engine-out soot and NOx emission values) and local values (i.e., LOL and flame evolution). Furthermore, an *ad hoc* methodology was employed to obtain a virtual soot NL signal starting from 3D-CFD variables, and the outcomes were compared against the experimental soot NL distributions and their spatially integrated values, thus obtaining an indirect validation of the complex and notoriously difficult-to-predict in-cylinder soot formation and oxidation processes.

2. Experimental setup

2.1. Optical engine, fuel-injection system, and operating conditions

The single-cylinder optical-engine configuration used for the experimental aspects of this study had 1.72-liter displacement, 125-mm bore, 140-mm stroke, and 12.0-MPa peak cylinder pressure. This configuration has been described in detail elsewhere [4,22]. The experimental data presented herein were acquired as part of the campaign described in [27], which employed a solenoid common-rail fuel injector with a four-orifice nozzle, an orifice diameter of 0.175 mm, and a spray umbrella angle of 140°. The DFI strategy used a four-duct module featuring a 3.0-mm duct inside diameter (D), 12.0-mm duct length (L), 3.0-mm gap (G) between the injector orifice outlet and the duct inlet plane, and a rounded duct inlet with a tapered duct outlet, i.e., a D3L12G3δ configuration [7]. The reader is directed to Figs. 1, 2, 4, and 5 of [22] for additional details regarding duct geometry and installation.

Data were acquired for both CDC and DFI combustion strategies with diesel fuel at two engine speed/load conditions: 10 bar $IMEP_g$ at 1200 rpm and 1 bar $IMEP_g$ at 700 rpm, each at two or three dilution levels, as described in [27]. The 1 bar $IMEP_g$ / 700 rpm condition is representative of idle, while the 10 bar $IMEP_g$ / 1200 rpm condition is representative of mid-load operation. Higher-load conditions could not be studied due to the 12.0-MPa peak cylinder pressure limit of the optical-engine configuration used for this work (the optical engine has been upgraded subsequently to enable operation to 20.0-MPa peak cylinder pressure [29]).

2.2. Optical diagnostics and post-processing

Simultaneous, high-speed images of natural luminosity (NL) and electronically excited hydroxyl-radical (OH*) chemiluminescence (CL) were acquired through a UV-grade synthetic fused-silica window in the bowl of the piston during the combustion events for each speed/load condition and combustion strategy. The NL images were acquired using a Photron SA-Z monochrome CMOS camera operating in 640 × 640-pixel format and fitted with a Nikon 105-mm, f/2.8, visible lens. A 600-nm short-wave-pass filter and a 3-mm-thick piece of Schott KG-3 filter glass were placed in front of the NL camera lens to suppress infra-red contributions from hot water vapor to the measured NL signal. The OH* CL images were acquired using a second Photron SA-Z monochrome CMOS camera operating in 640 × 640-pixel format and fitted with a Lambert HiCATT lens-coupled image intensifier with ultraviolet (UV) sensitive S20 photocathode and P46 phosphor (decays to 1% in 2 μs), a Nikon 105-mm f/4.5 UV lens, and a 310-nm bandpass filter. The NL and OH* CL cameras were arranged as shown in Fig. 2 of [4], and the resulting raw images were processed according to methods detailed therein to yield spatially integrated natural luminosity (SINL) and flame LOL, respectively, as functions of engine crank-angle. At least three engine runs were conducted at each operating condition, and a sequence of high-speed NL and OH* CL images was acquired for the first seven fired cycles of each run. By the seventh image sequence, the upper surface of the piston window typically became sufficiently fouled by soot deposition to warrant cleaning before the acquisition of further imaging data. It is worth specifying that both OH* CL and NL signals were highly repeatable from one cycle to the next at the conditions studied herein. Therefore, throughout the manuscript, only single-cycle experimental pictures will be presented to help appreciate potential differences between simulations and experiments.

3. Simulation methodology

3.1. Overview

The aim of this study is the development of a high-fidelity 3D-CFD numerical model for the SCORE under both CDC mode and DFI mode. This 3D-CFD activity was conducted on the commercially available software CONVERGE CFD 3.1 [33].

The 3D-CFD setup development process follows the same methodology as described in [34], thus including spray model calibration, full-cylinder cold-flow simulations, and sector combustion simulations.

3.2. Spray model

In this work, the spray was modelled though the Lagrangian particle tracking approach, whose sub-models were properly calibrated. Since the experimental spray data were not available for the injector used in the engine experimental campaign, the calibration process was carried out against the Engine Combustion Network (ECN) “Spray D” conditions [35,36], given the similar nozzle hole geometry. The injected fuel, both liquid and vapor phases, is n-dodecane. Concerning the grid settings, the domain was meshed with a Cartesian grid reaching 0.125 mm of minimum grid size through both fixed refinement regions and the adaptive mesh refinement (AMR) technique [33]. The detailed list of spray sub-models is reported in Table 2.

Fig. 1 reports the outcomes of the calibrated spray model in terms of liquid and vapor penetrations compared to the experimental data (both

Table 2
3D-CFD spray model setup.

Turbulence model	RANS - Standard k-eps [37] (with round-jet correction [38])
Liquid injection	Blob Model [39]
Droplet turbulent dispersion	O'Rourke model [40]
Spray Breakup	KH-RT model [41]
Evaporation	Frossling with boiling model [40]
Droplet drag	Dynamic drop drag [42]
Collision model	NTC collision model [43]

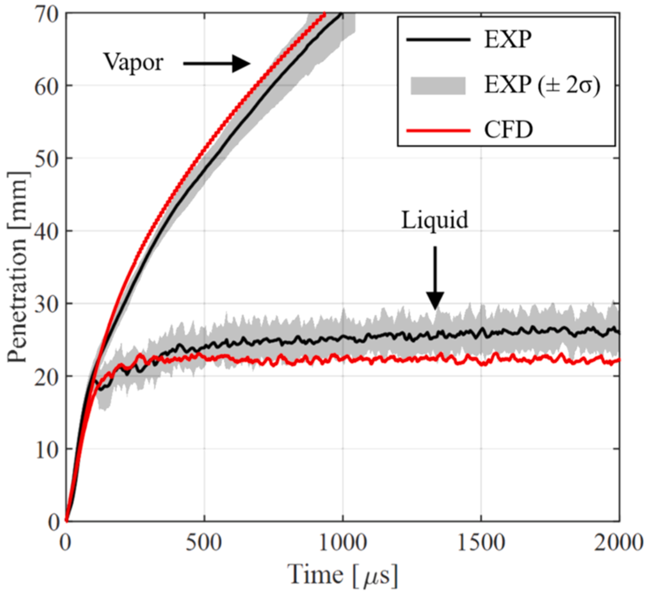

Fig. 1. Experimental (black) and 3D-CFD (red) liquid and vapor penetrations as a function of time, with solid lines representing the average values and shaded bands representing the standard deviation. Operating conditions: $T_{inj} = 363$ K, $P_{inj} = 1500$ bar, $T_{back} = 900$ K, $P_{back} = 60$ bar. Experimental data taken from [36].

average values and standard deviation bands). The simulated liquid penetration is defined as the radius of a sphere centred in the nozzle hole which contains 99% of the total liquid mass at each time instant, while the simulated vapor penetration is the longest distance between the nozzle hole and the cells which feature a fuel vapor mass fraction higher than 0.1%.

Generally, good agreement is obtained between simulation and experiment, with well-captured transient behaviors for both the predicted liquid and vapor penetrations curves which fall in the experimental standard deviation band for most of the time. Although the stabilized liquid length is slightly underestimated, the error with respect to the experimental standard deviation band can be considered acceptable, especially because lower values for stabilized liquid length have been measured by other studies under the same Spray D conditions [44, 45]. In light of this, this 3D-CFD spray model was employed in the subsequent engine simulations.

3.3. Full-cylinder cold flow simulation

Since the experimental optical engine was operated in a skip-fired mode, the full-cylinder cold flow simulations were initialized to simulate the gas exchange process between the last skip-fired cycle and the firing cycle, from the exhaust valve opening (EVO) up to the end of the compression stroke. An overview of the simulated full-cylinder geometry is reported in Fig. 2. Concerning the boundary conditions for the intake and exhaust flows, species concentration, temperature, and pressure values were provided at the tank level by creating two semi-spheres positioned upstream and downstream of the intake and exhaust runners, respectively. The diameters of these semi-spheres were set to three times the equivalent runner diameter. The heat transfer was described by the O'Rourke and Amsden model [46].

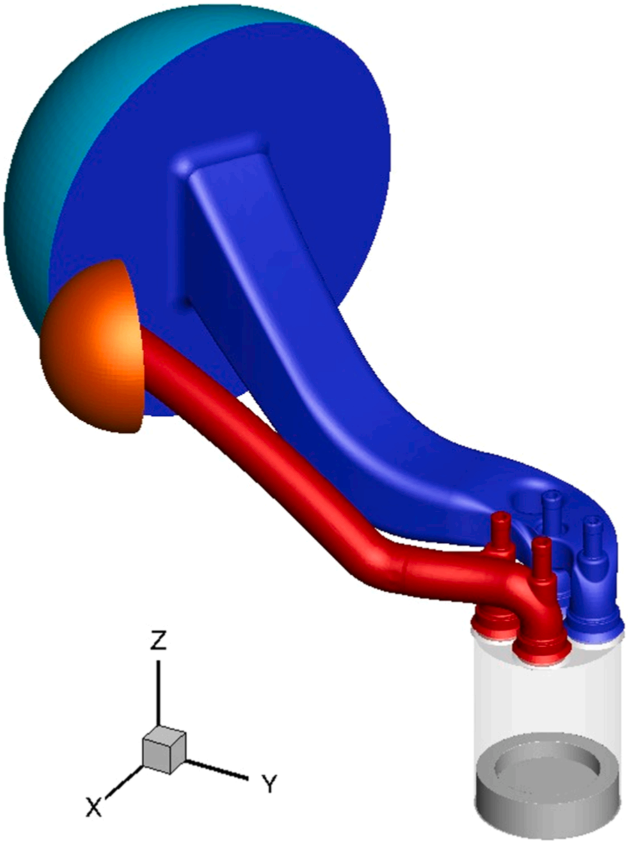

Fig. 2. Full-cylinder geometry for the 3D-CFD setup. The intake port and valves are shown in blue, while the intake flow boundary is in light blue. The exhaust port and valves are shown in red, while the exhaust outflow boundary is in orange. The in-cylinder region is colored gray. The image is taken at IVC (−153 deg aTDCf).

The outcomes of this 3D-CFD setup showed good agreement with experimental measurements in terms of in-cylinder trapped mass and pressure values during compression stroke for both CDC and DFI.

Fig. 3 shows the tangential velocity distribution at start of injection (SOI) for both CDC and DFI configurations. The comparison reveals differences in the flow field, with the DFI configuration exhibiting lower tangential velocity near the injector. From these simulations, two different variable mappings at intake valve closure (IVC) were extracted to initialize the corresponding sector combustion simulations. Given the inherent variability among sectors, the most representative ones in terms of temperature, pressure, and turbulence have been chosen by comparison with the full-cylinder average values.

3.4. Sector combustion simulation

Sector combustion simulations were performed from IVC to EVO. The computational domain was meshed with a Cartesian grid featuring a base grid size of 1 mm and a minimum grid size of 0.125 mm for the CDC and 0.0625 mm for the DFI. In particular, fixed refinements were applied to the cylinder walls (up to 0.5 mm), to the injector (up to 0.125 mm) and, for the DFI configuration, also in the duct region. Furthermore, the AMR technique was adopted leading to local refinements based on temperature gradients (up to 0.25 mm), on velocity gradients (up to

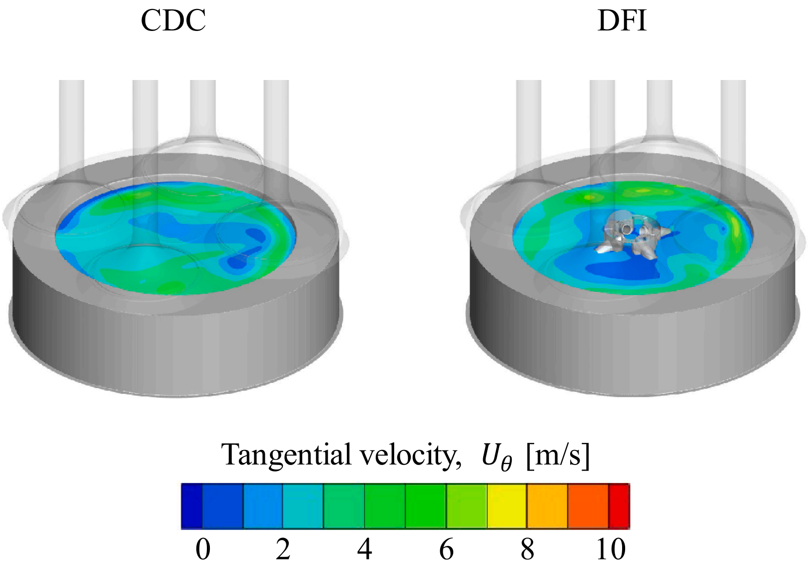

Fig. 3. Tangential velocity U_θ at SOI for both CDC (left) and DFI (right) in a horizontal plane passing through the center of the duct exit (same height for CDC). Working point: 10 bar IMEPg at 1200 rpm and 16% O_2 concentration.

0.125 mm), and on $y+$ values at the duct wall (up to 0.0625 mm). This latter was important to correctly describe flow/wall interaction inside the duct by means of the wall function, forcing $y+$ to locally remain in the range between 30 and 100. A sketch of the mesh structure highlighting each refinement technique is reported in Fig. 4, considering a time instant during the injection event (5 deg aTDCf).

The in-cylinder turbulence is described by the Reynolds-averaged Navier-Stokes (RANS) Standard k-ε model with the so-called “round jet correction” ($C_{\varepsilon 1} = 1.55$), commonly known to better predict the jet penetration [38], as in the spray simulations. For engine simulation, the liquid phase is introduced into the computational domain as Diesel#2, transitioning to n-heptane upon evaporation. For the combustion process, the SAGE detailed chemistry solver was employed, with the Skeletal Zeuch combustion mechanism for n-heptane (n-C_7H_{16}) [47]. Due to the PAH reactions embedded in this mechanism, the detailed particulate mimic model [48] was utilized for soot emissions computation. For NOx emissions, the thermal NOx model based on Zel’dovich reactions was employed [49]. It is worth noting that the final model is the same for both CDC and DFI configurations, with no specific adjustments made for the different configurations. A summary of the models used in the sector model setup is reported in Table 3.

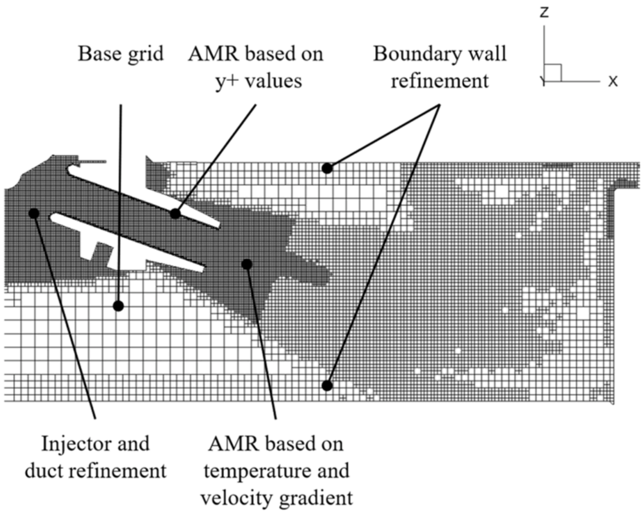

Fig. 4. Mesh adopted for sector combustion simulations, in DFI configuration, during fuel injection (5 deg aTDCf) on a plane containing the cylinder axis and the duct axis.

3.5. Post-processing methodology

The model validation has been performed analyzing both macroscopic quantities (e.g., pressure trace, burn rate, engine-out emissions) and local quantities (e.g., flame evolution, LOL, soot NL).

Regarding local quantities, the need for a consistent comparison against experimental data led to the utilization of *ad hoc* post-processing procedures for both flame visualization and CFD-derived soot natural luminosity. Indeed, first, CFD flame evolution was compared with OH* chemiluminescence images, then, CFD soot concentrations were compared with soot natural luminosity images.

3.5.1. Flame visualization

To enable a consistent comparison with the experimental OH* chemiluminescence, the 3D data were first interpolated onto a homogeneous structured grid with cells dimensions equal to the optical images’ pixel size. Then, similarly to [51], the OH mole fraction was integrated over the total cell volume along the line-of-sight (LOS, i.e., distance in the z-direction from the top of the piston window to the firedeck), thus obtaining a two-dimensional projection of the flame. In other words, assuming that the experimental OH* chemiluminescence intensity is proportional to its concentration along the LOS, the absolute mole number of OH molecules along each LOS (Eq. (1)) was employed to reconstruct the planar flame visualization.

$$OH_{moles,\ projected} = \int_{LOS} n_{OH} dV \tag{1}$$

It is worth highlighting that the ground-state OH concentration was herein used instead of the OH* radicals concentration, since the latter

Table 3
3D-CFD setup summary for sector combustion simulations.

Turbulence model	RANS Standard k-ε [37] (with round jet correction [38])
Heat Transfer model	O’ Rourke and Amsden model [46]
Spray/wall interaction	Rebound/slide model [50]
Combustion model	SAGE detailed chemistry solver
NOx model	Extended Zel’dovich mechanism [49]
Soot formation/ oxidation	Particulate Mimic model [48]

specie was not available in the validated combustion mechanism. Consequently, it was assumed that there is a thermal equilibrium between OH and its excited counterpart OH*, as in [52].

Concerning the computation of the flame LOL, it was instead determined as the *"first axial location of the Favre-averaged OH mass fraction reaching 2% of its maximum in the domain"*, according to the ECN modelling standards [35].

3.5.2. CFD-derived soot natural luminosity

A proper post-processing methodology was adapted from [53] to replicate soot NL starting from the outputs of the 3D-CFD simulations. Despite the strong relationship between the intensity of the NL signal in a given region and the amount of soot in the same region, other physical quantities also play a role. A particle of soot, indeed, is characterized by its own emissivity, and the emissivity of a particle depends on its temperature [54]. Furthermore, transmissivity, camera spectral response as well as the position of the camera play an important role. For this reason, all these effects were taken into account in the developed methodology.

The intensity of radiation of a soot particle can be computed as in Eq. (2):

$$I_{soot} = I_{bb} {}^{*} \varepsilon_{soot} \tag{2}$$

where I_{bb} denotes the intensity of radiation of a black body, and ε_{soot} is the soot particle emissivity. I_{bb} can be computed according to the Planck's law (Eq. (3)):

$$I_{bb} = \frac{C_1}{\lambda^5 \left[e^{\left(\frac{C_2}{\lambda T}\right)} - 1 \right]} \tag{3}$$

where $C_1 = 1.1910439 \cdot 10 - 16\ W \cdot m2\ /sr$ and $C_2 = 1.4388 \cdot 10 - 2\ m \cdot k$ (both from [55]), λ is the signal wavelength in m, and T is the soot particle temperature in K. ε_{soot} has been computed as in Eq. (4) [53]:

$$\varepsilon_{soot} = 1 - \exp\left(- \frac{g f_v L_{CFD}}{\lambda^{\alpha}} \right) \tag{4}$$

With $g = 6.3\ \mu m^{-1}$ [53], f_v soot volume fraction, L_{CFD} the length of the considered cell in m, and α empirical function dependent on the considered wavelength, expressed by Eq. (5) [53]:

$$\alpha = 1.22 - 0.245 {}^{*} ln(\lambda[\mu m]) \tag{5}$$

Since the target intensity of radiation is not related to a single isolated computational cell but to a cell within a three-dimensional domain, it is crucial to account for the contribution from adjacent cells along the same LOS. This represents a group of cells with the same x and y coordinates but varying z-positions. As a result, for each cell of a given LOS the intensity of radiation can be derived as the one of the cell itself plus the contribution of the cell upstream of the signal direction, influenced by the transmissivity of the soot particles inside the cell. This logic was implemented in an integration process that begins with the first cell at the bottom of the combustion chamber, moves towards the cylinder head, and then returns towards the bottom of the chamber, whose final signal is the one recorded by the camera. The reflectivity index (ρ_{wall}) of the cylinder head was also taken into account for the cell adjacent to the head wall. A schematic representation of this integration process is provided in Fig. 5, taken from [55]. Finally, this integration process was executed over the relevant wavelength range, incorporating the camera's spectral response (C_λ) and the area of the optical window (A), as in Eq. (6):

$$NL_{CFD} = \int_{400\ nm}^{650\ nm} (I_{\lambda,out} \cdot A \cdot C_\lambda) d\lambda \tag{6}$$

For this work, the relevant wavelengths range was set to 400–650 nm, consistently with the experimental setup.

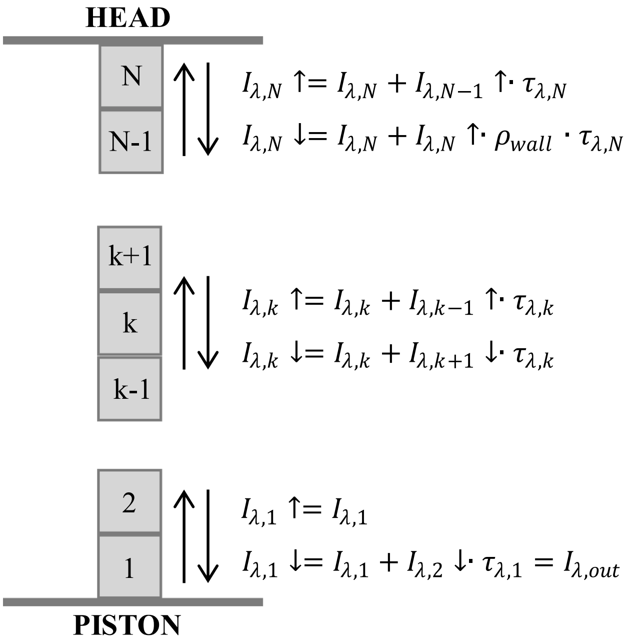

Fig. 5. Scheme for the line-of-sight (LOS) integration. Reproduced from [55].

It is noteworthy that the CFD SINL signal was then obtained by simply spatially integrating the 2D NL distribution resulting from the described procedure.

For the sake of clarity, it is important to point out the assumptions that have been introduced in the present methodology. First, since soot was considered as an aerosol species uniformly distributed within each computational cell, as also applied in [53], the soot particle temperature was assumed equal to the mean temperature of the computational cell. Although this choice eliminates potential temperature differences between soot particles and surrounding gas, a temperature difference lower than 1 K was observed under thermal equilibrium between gas and soot in [56]. Second, the emitted radiation was attributed exclusively to soot, thus neglecting contributions from other species present in the cell. In other words, the surrounding gas was assumed to be completely transparent. Third, assuming a sufficiently large distance between emitters and detector, soot particles were assumed to emit light only in the vertical direction, thus neglecting their homogeneous directionality and the resulting multiple scattering effects. Accordingly, the total intensity of radiation for each cell was computed as the sum of its own contribution and that of adjacent cells along the LOS, while neglecting contributions from all other directions.

4. Results

This section presents the validation of the model across all the available working points, focusing on the model's capability to predict main combustion results, engine-out emissions, and soot formation/oxidation processes.

4.1. Combustion and flame evolution

In Figs. 6 and 7, experimental and predicted pressure traces and burn rates at the medium load condition are reported for CDC and DFI, respectively, for each oxygen concentration available (21%, 18%, and 16% for CDC; 16% and 14% for DFI). Accurate predictions are achieved for both configurations at each oxygen concentration level. Indeed, ignition delay (ID), premixed combustion intensity and late combustion

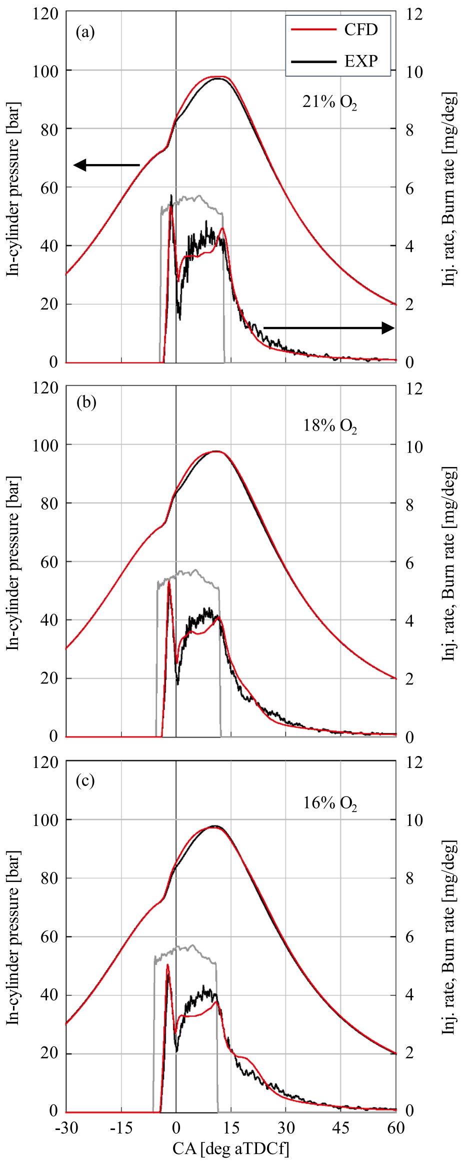

Fig. 6. Injection rate (gray), experimental (black) and 3D-CFD (red) in-cylinder pressure and burn rate under CDC conditions at 10 bar IMEPg and 1200 rpm for 21% (a), 18% (b), and 16% (c) oxygen concentration. Black arrows indicate the reference y-axis.

phase are well replicated by the model, and only the mixing-controlled combustion phase is slightly underestimated. This underestimation might be attributed to the use of a slightly different injector during spray calibration, as abovementioned (i.e., “spray D” featuring similar geometry with the injector under investigation, for which experiments were not available).

The introduction of a duct in the domain does not introduce any reduction of the accuracy of the model, highlighting its reliability.

The good agreement between experimental data and simulation results can be observed also in Fig. 8, presenting the comparison between the simulated and the experimental main combustion parameters (combustion anchor angle, MFB50 (a); combustion duration, MFB10–75 (b); maximum pressure value (c) and phasing (d)) as correlation plots for both CDC and DFI configurations.

In Fig. 9, experimental and simulated ID values are collected for both CDC and DFI as a function of the oxygen concentration level. As can be seen, the simulation well predicts both absolute values and trends changing dilution or configuration, showing a maximum error lower than 0.5 deg. In particular, the DFI configuration consistently exhibits a longer ID which leads to a more pronounced premixed burn, as depicted in Fig. 10, where CDC and DFI pressure and burn rate traces are compared for both experiments and simulations for the case with 16% oxygen concentration. As can be observed, the simulations successfully capture also the other main macroscopic features of DFI combustion with respect to the CDC, such as the more intense mixing-controlled combustion phase and the faster burn-out, resulting in slightly higher maximum pressure values.

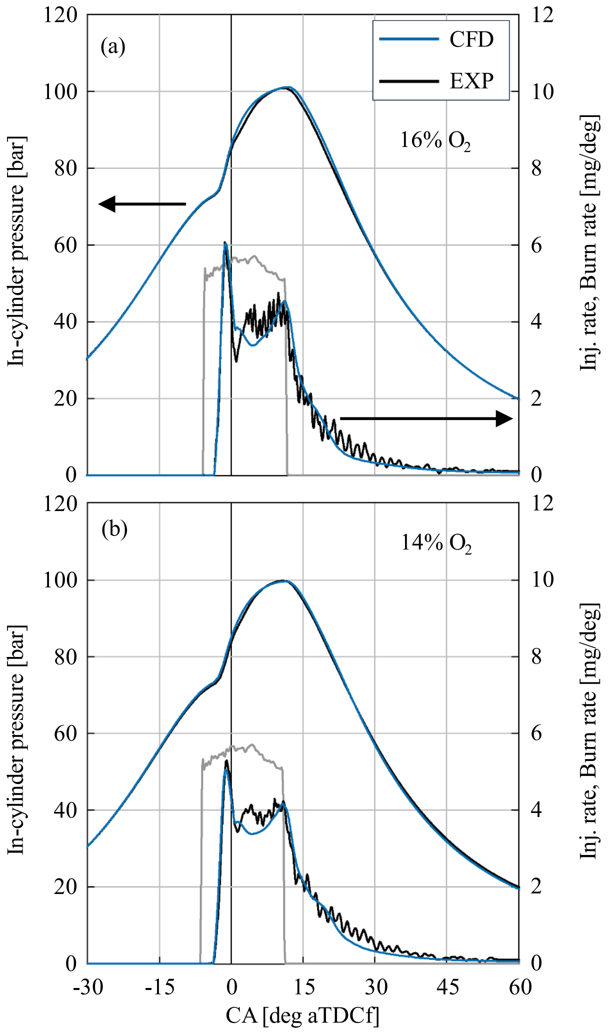

Fig. 7. Injection rate (gray), experimental (black) and 3D-CFD (blue) in-cylinder pressure and burn rate under DFI conditions at 10 bar IMEPg and 1200 rpm for 16% (a) and 14% (b) oxygen concentration. Black arrows indicate the reference y-axis.

Looking at the flame local evolution inside the combustion chamber, in Fig. 11 the $OH_{moles,\ projected}$ distribution against the corresponding experimental OH* chemiluminescence is reported for both CDC and DFI after the end of the injection (i.e., 12.5 deg aTDCf). It is noteworthy that the CFD flames are mirrored from the single sector outcome for visualization purposes.

In general, the flame evolution is well described, showing high similarity between experimental images and CFD-derived ones for both CDC and DFI configurations. Notably, the flame-to-flame interaction regions exhibit higher luminosity compared to the injection axis region, a characteristic captured in both experimental and CFD images. Additionally, in experimental OH luminosity images, the near-wall regions

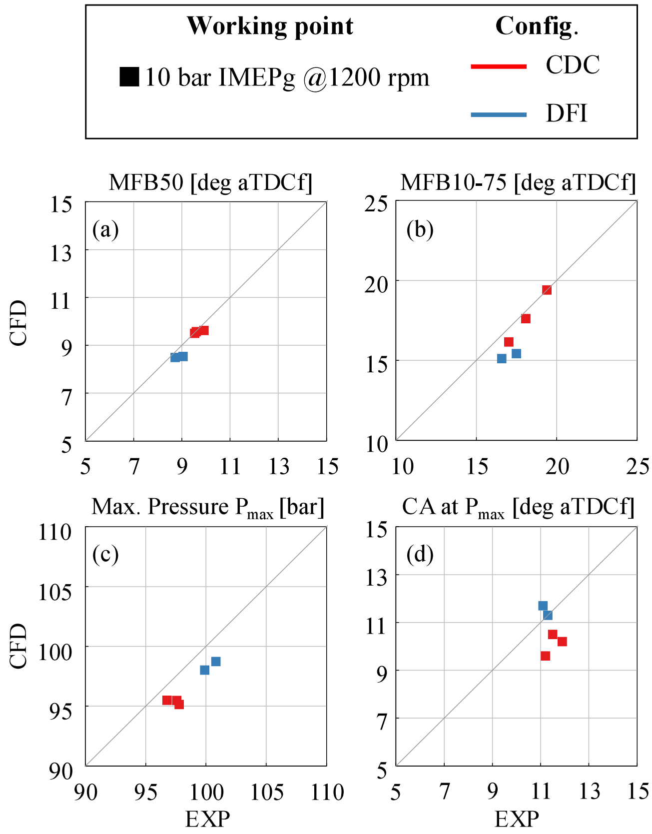

Fig. 8. Main combustion parameters correlation plots between experimental data and simulation results with oxygen concentration sweep: MFB50 (a); MFB10–75 (b); pressure peak value (c); crank angle at pressure peak value (d), for both CDC (red) and DFI (blue) configurations. Working point: 10 bar IMEPg at 1200 rpm.

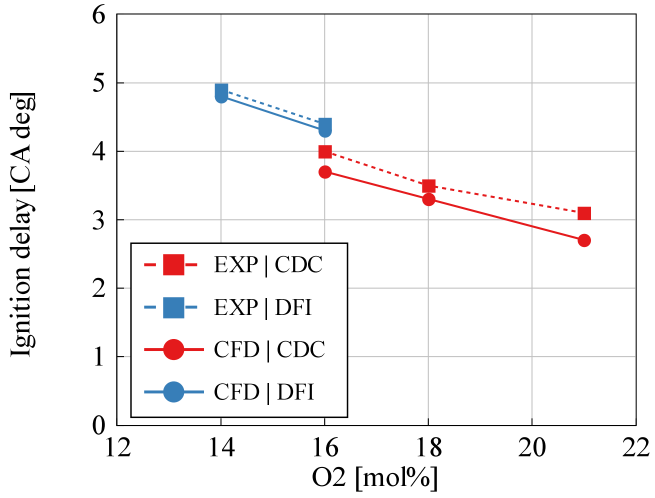

Fig. 9. Experimental (dashed line and square marker) and 3D-CFD (continuous line and circle marker) ignition delay for both CDC (red) and DFI (blue) as a function of O₂ concentration. Working point: 10 bar IMEPg at 1200 rpm.

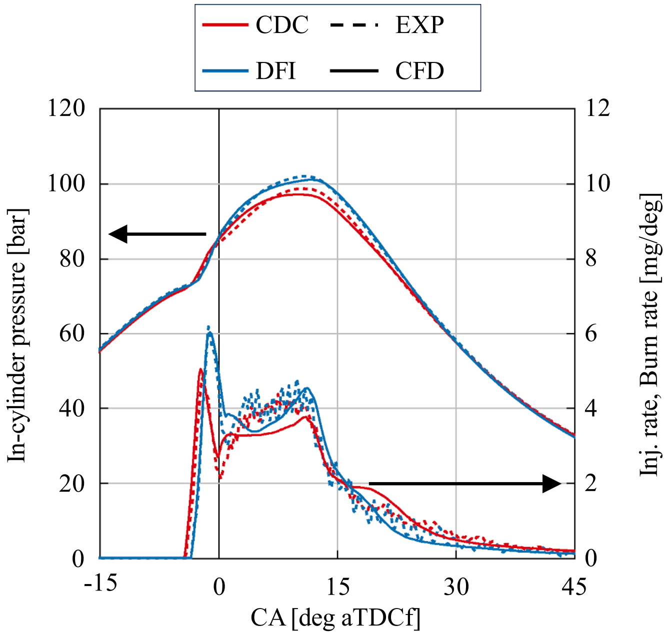

Fig. 10. In-cylinder pressure and burn rate for both CDC (red) and DFI (blue) at 10 bar IMEPg and 1200 rpm (16% O_2), with experimental results shown as dashed lines and 3D-CFD simulation results as solid lines. Black arrows indicate the reference y-axis.

exhibit almost negligible luminosity for both CDC and DFI configurations while the CFD-derived images show the flame attached to the walls. This discrepancy could be attributed to experimental visualization being hindered by contamination, such as deposits on the optical window, which may obscure the near-wall regions.

Comparing CDC and DFI, differences emerge in the flame behavior: the DFI exhibits a higher degree of flame recirculation, with the flame propagating back toward the injector region faster. This behavior is observable in both simulation and experimental pictures to a similar extent. It is worth noting that, since this increased recirculation can lead to re-entrainment of hot combustion products in the duct in cases of relatively long injection durations [23], its correct prediction is important. Additionally, both experimental and CFD-derived images show that DFI features a longer LOL than CDC. To provide a broader overview on this latter aspect, in Fig. 12, a quantitative comparison of the experimental and predicted LOL values at the end of the premixed burn (EOPMB) and the end of the injection (EOI) are reported for both CDC and DFI at each oxygen concentration level. The experimental LOL data shown in Fig. 12 have been arithmetically averaged and standard deviations calculated over each of the four sprays and for seven to 21 replicates at the crank angle of interest, for a total of 28 to 84 individual measurements at EOPMB and at EOI. CDC at 21% O_2 had seven replicates; CDC 18% O_2, CDC 16% O_2, and DFI 16% O_2 had 14 replicates each; and DFI 14% O_2 had 21 replicates.

Generally, the main trends changing dilution or configuration are respected, such as higher LOL when dilution increases and when the duct is implemented in front of the injector tip. At EOPMB, LOL values are correctly captured apart from a certain underestimation for the CDC at 18%. At the EOI, a general underestimation is present for analyzed cases, but the differences remain within a reasonable range, thus highlighting the reliability of the CFD model. Specifically, the error observed in the CFD simulations is below 5 mm, lower than the experimental deviation interval (expressed by the 2-sigma deviation in Fig. 12). Considering the 16% O_2 case in DFI configuration, it is possible to notice how the CFD-derived LOL at the EOI is anchored to duct exit (i.e., about 15 mm), differently from experiments, where an approximately 4-mm gap between duct outlet and autoignition region seems preserved. The underlying reasons behind this behavior are currently under study to improve model predictions: the unsuited spray model and the neglected turbulence-chemistry interaction could explain these discrepancies [11]. However, this difference does not impact in a significant way the DFI capability to abate soot formation according to the model, also because this does not generate any detrimental in-duct combustion

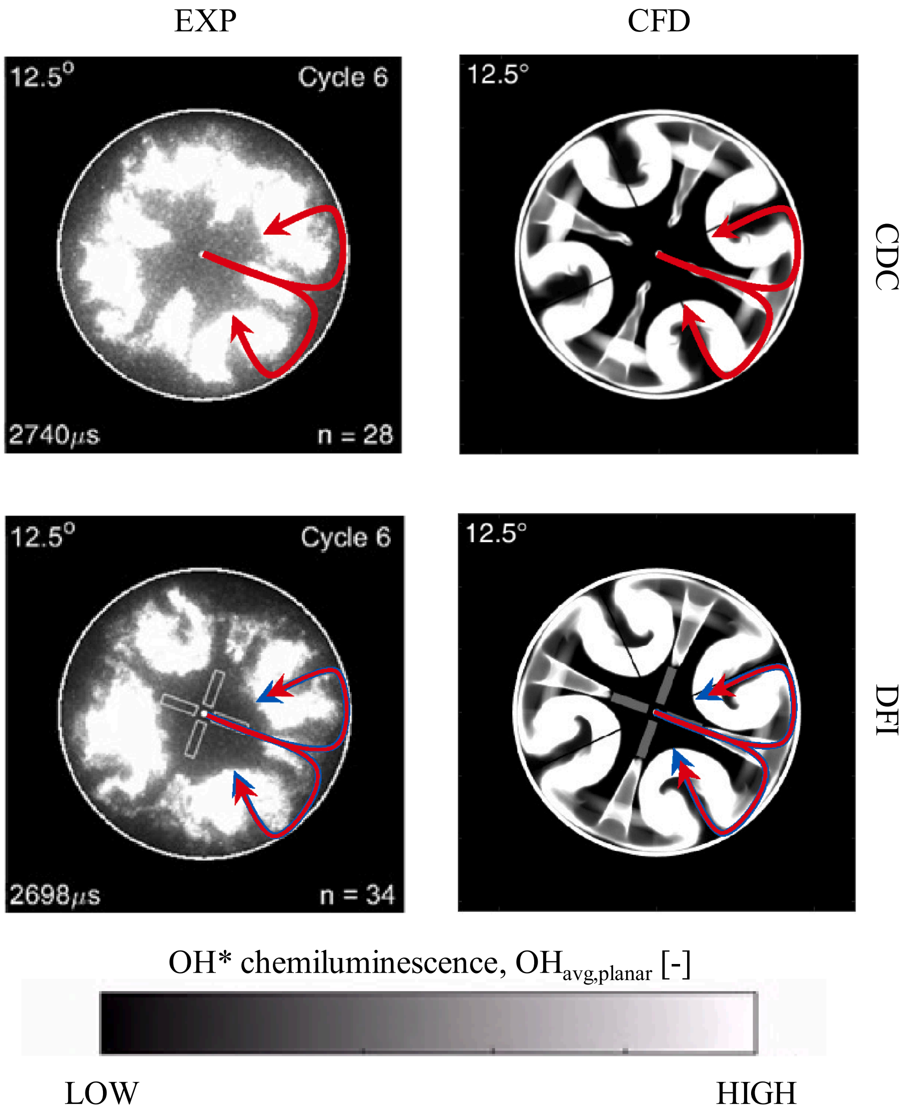

Fig. 11. Experimental (left) OH* chemiluminescence images for CDC and corresponding CFD-derived OH distributions (right) for both CDC (top) and DFI (bottom) configurations at 12.5 deg aTDCf illustrating the flame recirculation (red arrows for CDC, blue arrows for DFI). CFD flames are mirrored for improved visualization. Working point: 10 bar IMEPg, 1200 rpm, and 16% O_2.

event, as known in the literature [13,14].

Finally, the CFD model effectively captures the overall flame evolution, and the key phenomena associated with both configurations, providing valuable insights into their respective behaviors.

4.2. Emissions and CFD-derived soot natural luminosity

Fig. 13 presents the experimental and simulated engine-out soot/NOx trade-off with dilution, in terms of indicated specific emissions, for both CDC and DFI. The values were normalized with respect to the CDC case at 16% O_2.

In general, the emissions values are well captured for both configurations, with good agreement in terms of NOx and soot apart from the CDC case at 21% O_2, which is underestimated by the model. This underestimation may be linked to the soot reaction chemistry of the employed skeletal combustion mechanism, which was employed over a relatively large range of oxygen concentrations. The main trends are also respected by the model, such as the opposite behavior of soot and NOx emissions when the O_2 concentration changes, and the impact of the duct presence on both soot and NOx. Regarding this latter point, the model reasonably predicts the remarkable soot reduction when transitioning from CDC to DFI: 72% reduction for CFD against 80% reduction for experiments at 16% O_2. The model also captures the higher NOx levels observed for the DFI configuration in comparison with the CDC: 3% increase for CFD against 15% increase for experiments at 16% O_2, consistent with the more intense premixed burn. Therefore, even though some underestimations are present, the model was considered robust in predicting emissions, since it was capable to capture the main behaviors of the soot/NOx trade-off.

To assess the capability of the model to predict the in-cylinder soot formation and oxidation processes, Fig. 14 shows the experimental NL images against the corresponding CFD-derived NL distributions, computed according to the methodology explained in Section 3.5, for both CDC and DFI configurations at 16% O_2. Four time instants were selected for the comparison during both soot-formation and soot-oxidation phases. It is worth noting that, for experiments, single-cycle experimental data are shown rather than ensemble-averaged one.

In general, the CFD predictions are in good agreement with the experimental images for both CDC and DFI configurations, effectively capturing the temporal evolution of soot luminosity at all considered time instants. For both configurations, the CFD images accurately reproduce the increased soot luminosity observed between 2 and 10 CA

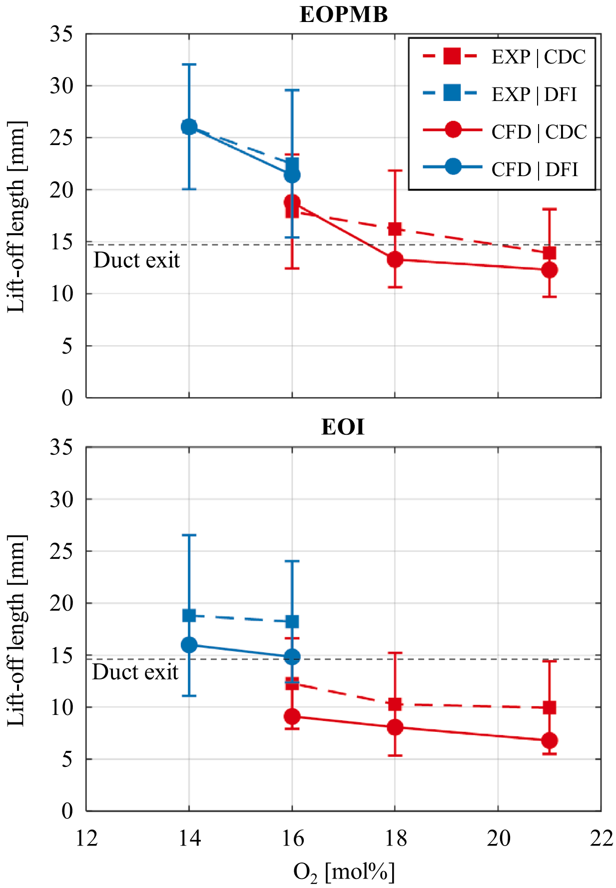

Fig. 12. Experimental (dashed line and square marker) with 2-sigma deviation bars and 3D-CFD (continuous line and circle marker) lift-off length (LOL) for both CDC (red) and DFI (blue) as a function of O_2 concentration: (top) end of premixed burn (EOPMB), (bottom) end of injection (EOI). Duct exit position highlighted with horizontal black dashed lines. Working point: 10 bar IMEPg at 1200 rpm.

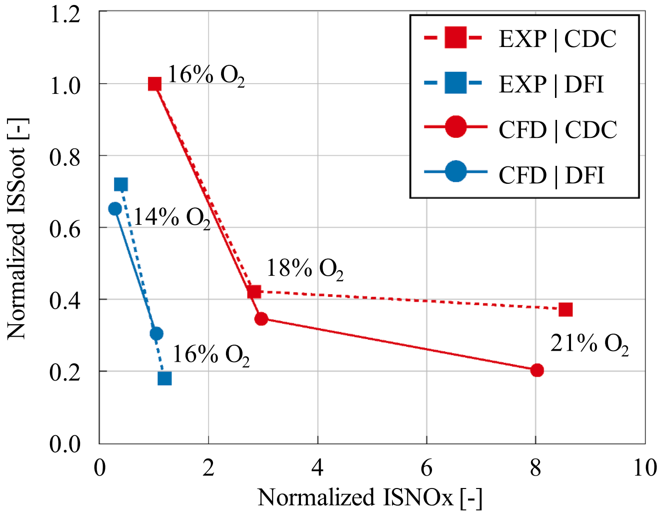

Fig. 13. Normalized experimental (dotted line) and 3D-CFD (solid line) soot/NOx trade-off for both CDC (red) and DFI (blue) configurations, varying O_2 concentration level. Working point: 10 bar IMEPg at 1200 rpm.

deg aTDCf, which corresponds to a phase where the soot formation rate is dominant over the oxidation rate. Looking at 20 CA deg aTDCf, both CDC and DFI configurations show higher soot luminosity in the region where the flames interact while near-zero luminosity in the injector axis region is present. This common feature indicates that the interaction between the two flames as well as the entrainment processes after the EOI are well represented in both cases.

Furthermore, the robustness of the model is highlighted in capturing the differences in the soot behavior between CDC and DFI, which are similar to the ones emerging from experimental images. For instance, at 10 CA deg aTDCf, the model correctly replicates the stronger flame-to-flame interaction in the DFI case, leading to larger luminosity differences between the center and the side of each flame. This behavior is driven by the abovementioned faster flame recirculation which leads to soot clouds closer to the center of the chamber for the DFI, near the duct exit at 20 CA deg aTDCf for both experimental images and CFD predictions. Although the injection is over by this time (see Figs. 6 and 7), the prediction of this aspect is important because it could negatively impact the soot oxidation process due to the lower temperatures in the duct region (due to heat losses to the ducts) and reduced oxygen availability (due to the volume occupied by the duct assembly). Moreover, at this time instant, the overall soot luminosity trend begins to diverge between CDC and DFI, with the luminosity starting to decrease for DFI, whereas for CDC it continues to increase in both experiments and simulations. Indeed, at 30 CA deg aTDCf, soot NL is nearly absent in the DFI case, while CDC still exhibits residual luminosity with the soot concentrated in a single central cloud, according to both experimental observations and CFD predictions.

In order to have a more quantitative description of the NL intensity in the combustion chamber, the experimental and simulated SINL is shown in Fig. 15 for both CDC and DFI at each O_2 concentration level. Experimental and CFD curves have been normalized with respect to the corresponding maximum value of the CDC case at 16% O_2.

Focusing on the CDC, the CFD SINL curves at each O_2 level are very similar to the experimental ones in terms of both values and temporal windows, confirming the reliability of the model and the effectiveness of the NL post-processing procedure. When transitioning to the DFI analysis, the trend of SINL with O_2 was well-captured by the CFD model, although some slight discrepancies emerge in terms of absolute values compared to the CDC and comparing the temporal window between the 16% and the 14% O_2 level. These discrepancies could be related to lower predicted flame temperatures in the DFI case, due to the underestimated LOL compared to the experimental data. However, it is worth noting that the experimental and numerical SINL curves start to fall at a very similar time instant, thus pointing out the correct representation of the balance between soot formation and oxidation for each oxygen concentration also for the DFI case study. Moreover, as mentioned above, the reduction of the SINL temporal window moving from CDC to DFI at 16% O_2 is correctly reproduced by the model.

In conclusion, the overall good agreement between experiments and simulations indicates that, on the one hand, the developed CFD model of the optical engine effectively captures the main characteristics of the soot formation and oxidation processes, substantiating its reliability for predictive analyses; on the other hand, the presented methodology to derive soot NL values from CFD can effectively work, potentially giving robustness to models thanks to accurate validation against optical images, and paving the way to large improvements in the development of high-fidelity CFD models for CI engines and diesel combustion in general.

5. Conclusions

The aim of this work is the development of a high-fidelity computational fluid dynamics (CFD) model for the Sandia Compression-Ignition Optical Research Engine (SCORE) under both conventional diesel combustion (CDC) mode and ducted fuel injection (DFI) mode. For this purpose, the same model (without any adjustment when conditions changed) was thoroughly validated against experimental data

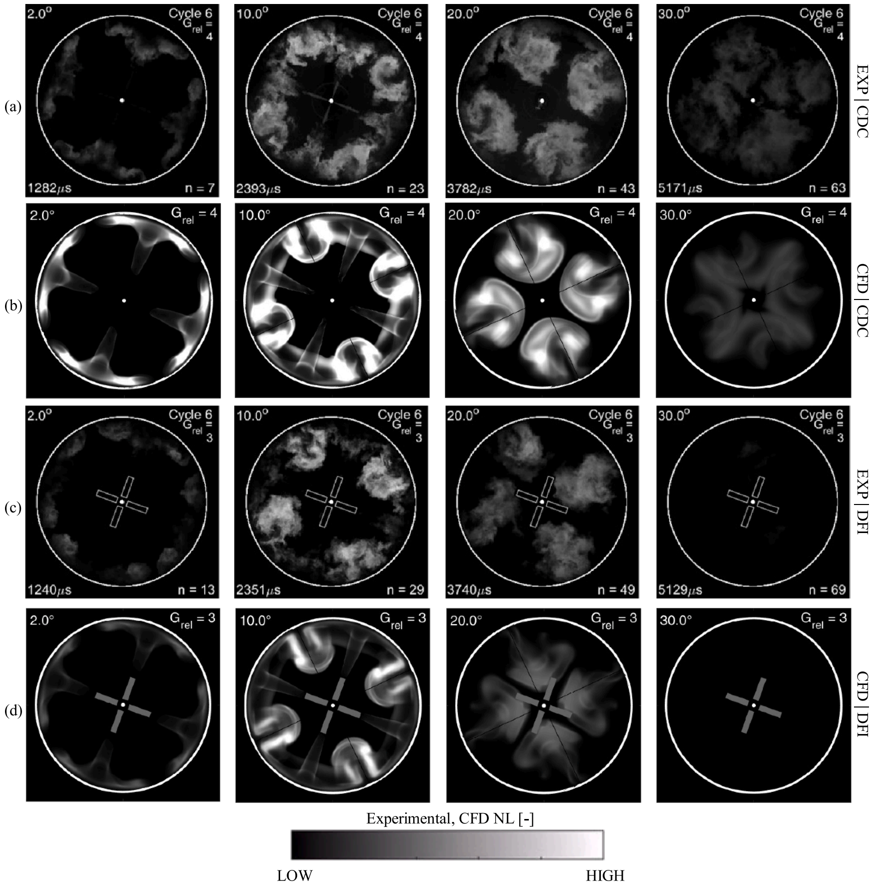

Fig. 14. (a) Soot natural luminosity (NL) for CDC, (b) corresponding CFD-derived NL images, (c) experimental soot natural luminosity for DFI, and (d) corresponding CFD-derived NL images for four time instants (2, 10, 20, and 30 deg aTDCf) at 10 bar IMEPg, 1200 rpm, and 16% O₂. Videos for each oxygen concentration are available in the Supplementary material.

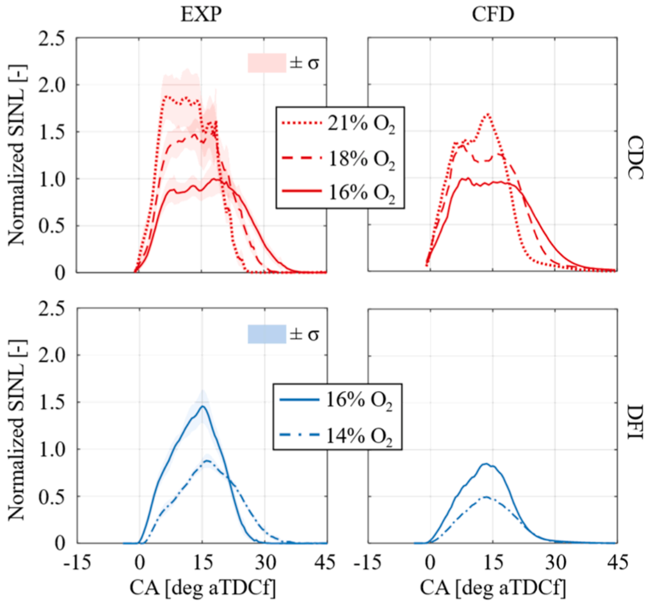

Fig. 15. Experimental (left) with standard deviation and CFD-derived (right) spatially integrated natural luminosity (SINL) as a function of crank angle for CDC (top) and DFI (bottom) at various O₂ concentrations: 14% (dash-dotted line); 16% (solid line); 18% (dashed line); 21% (dotted line). Working point: 10 bar IMEPg at 1200 rpm.

related to two load conditions (10 bar IMEPg at 1200 rpm and 1 bar IMEPg at 700 rpm), two configurations (CDC and DFI), and four oxygen concentrations (14%, 16%, 18%, and 21%). Key findings of the validation process follow.

- Macroscopic combustion behavior: the model successfully captured main combustion characteristics in terms of pressure traces and burn rate for each working point, O_2 concentration, and configuration.
- In-cylinder flame evolution: the flame structure and lift-off length (LOL) were well predicted, validating the model's ability to replicate in-cylinder flow-field and combustion characteristics.
- Soot-NOx trade-off with dilution: simulated results accurately reproduced the trade-off, simultaneously capturing the impact of the O_2 concentration variation and of the duct presence.
- Soot natural luminosity (NL): a novel methodology was developed to replicate soot NL using 3D-CFD outputs (e.g., soot volume fraction, temperature, etc.). This enabled a visual comparison with optical NL images, contributing to the model validation in terms of in-cylinder soot formation and oxidation processes for each configuration and O_2 concentration level. This model validation methodology is one of the major innovative outcomes of the present study. This thoroughly validated model can thus be exploited for high-fidelity predictive analysis for improved understanding and optimization of DFI technology.

In conclusion, the model demonstrated strong predictive capabilities for both CDC and DFI analysis, accurately replicating key phenomena. This suggests its suitability for future investigations, such as duct geometry optimization, engine virtual calibration, and impact of multiinjection strategies with DFI.

Abbreviations

3D	3-dimensional
AMR	Adaptive mesh refinement
aTDCf	After top dead center firing
CDC	Conventional diesel combustion
CFD	Computational fluid dynamics
CI	Compression-ignition
DFI	Ducted fuel injection
ECN	Engine Combustion Network
EGR	exhaust gas recirculation
EOI	End of injection
EOPMB	End of premixed burn
EVO	Exhaust valve opening
ID	Ignition delay
IMEPg	gross indicated mean effective pressure
IVC	Intake valve closure
KH-RT	Kelvin–Helmholtz and Rayleigh–Taylor
LLFC	Leaner lifted-flame combustion
LOL	Lift-off length
LOS	line-of-sight
MFB	Mass fraction burned
NL	Natural luminosity
NOx	Nitrogen oxides
RANS	Reynolds-averaged Navier-Stokes
SCORE	Sandia compression-ignition optical research engine
SINL	Spatially integrated natural luminosity
SOI	Start of injection

CRediT authorship contribution statement

C. Segatori: Writing – review & editing, Validation, Supervision, Project administration, Methodology, Investigation, Conceptualization. **M. Orlando:** Writing – original draft, Validation, Software, Methodology, Investigation, Formal analysis. **A. Piano:** Writing – review & editing, Supervision, Project administration, Methodology, Investigation, Conceptualization. **F. Millo:** Writing – review & editing, Resources, Project administration. **C.J. Mueller:** Writing – review & editing, Writing – original draft, Validation, Supervision, Resources, Investigation, Funding acquisition, Formal analysis, Conceptualization.

Declaration of competing interest

The authors declare that they have no known competing financial interests or personal relationships that could have appeared to influence the work reported in this paper.

Acknowledgements

The authors acknowledge the CINECA award under the ISCRA initiative, for the availability of high-performance computing resources and support.

Convergent Science provided CONVERGE licenses and technical support for this work.

CJM is grateful to the U.S. Department of Energy (DOE) Vehicle Technologies Office and Office of Technology Transitions for support of the research conducted at Sandia National Laboratories. The authors also thank Gustav Nyrenstedt, Christopher Nilsen, and Drummond Wengrove for their assistance with data acquisition. This article has been authored by an employee of National Technology & Engineering Solutions of Sandia, LLC, under Contract No DE-NA0003525 with DOE. The employee owns all right, title, and interest in and to the article and is solely responsible for its contents. The United States Government retains and the publisher, by accepting the article for publication, acknowledges that the United States Government retains a non-exclusive, paid-up, irrevocable, world-wide license to publish or reproduce the published form of this article or allow others to do so, for United States Government purposes. The DOE will provide public access to these results of federally sponsored research in accordance with the DOE Public Access Planhttps://www.energy.gov/downloads/doe-public-access-plan. This paper describes objective technical results and analysis. Any subjective views or opinions that might be expressed in the paper do not necessarily represent the views of the DOE or the United States Government.

Supplementary materials

Supplementary material associated with this article can be found, in the online version, at doi:10.1016/j.jaecs.2025.100408.

Data availability

Data will be made available on request.

References

[1] "New EU truck sales by power source." [Online]. Available: www.acea.auto.

[2] Morgan C, Goodwin J. Impact of the proposed euro 7 regulations on exhaust aftertreatment system design. Johns Matthey Technol Rev 2023;67(2):239–45. https://doi.org/10.1595/205651323X16805977899699.

[3] Boger T, Rose D, He S, Joshi A. Developments for future EU7 regulations and the path to zero impact emissions – a catalyst substrate and filter supplier's perspective. Transp Eng 2022;10:100129. https://doi.org/10.1016/j.treng.2022.100129.

[4] Polonowski C, Mueller CJ, Gehrke C, Bazyn T, et al. An experimental investigation of low-soot and soot-free combustion strategies in a heavy-duty, single-cylinder, direct-injection, optical diesel engine. SAE Int J Fuels Lubr 2012;5(1):51–77. https://doi.org/10.4271/2011-01-1812.

[5] Mueller CJ. Ducted fuel injection, 9. U.S. Patent; 2018. 909,549 B2.

[6] Mueller CJ, Nilsen CW, Ruth DJ, Gehmlich RK, et al. Ducted fuel injection: a new approach for lowering soot emissions from direct-injection engines. Appl Energy 2017;204:206–20. https://doi.org/10.1016/j.apenergy.2017.07.001.

[7] Gehmlich RK, Mueller CJ, Ruth DJ, Nilsen CW, et al. Using ducted fuel injection to attenuate or prevent soot formation in mixing-controlled combustion strategies for engine applications. Appl Energy 2018;226:1169–86. https://doi.org/10.1016/j.apenergy.2018.05.078.

[8] Segatori C, Piano A, Peiretti Paradisi B, Bianco A, et al. Exploiting the potential of large eddy simulations (LES) for ducted fuel injection investigation in non-reacting conditions. Int J Multiph Flow 2024;171:104686. https://doi.org/10.1016/j.ijmultiphaseflow.2023.104686.

[9] Millo F, Piano A, Peiretti Paradisi B, Postrioti L, et al. Ducted fuel injection: experimental and numerical investigation on fuel spray characteristics, air/fuel mixing and soot mitigation potential. Fuel 2021;289:119835. https://doi.org/10.1016/j.fuel.2020.119835.

[10] Nilsen C, Yraguen B, Mueller CJ, Genzale C, et al. Ducted fuel injection vs. Free-spray injection: a study of mixing and entrainment effects using numerical modeling. SAE Int J Engines 2020;13(5):705–15. https://doi.org/10.4271/03-13-05-0044.

[11] Lucchini T, Zhou Q, D'Errico G, Severgnini D. Modeling fuel-air mixing, combustion and soot formation with ducted fuel injection using tabulated kinetics. SAE Technical Paper 2022-01-0403; 2022. https://doi.org/10.4271/2022-01-0403.

[12] Guo J, Brouzet D, Chung WT, Ihme M. Analysis of ducted fuel injection at high-pressure transcritical conditions using large-eddy simulations. Int J Engine Res 2024;25(2):305–19. https://doi.org/10.1177/14680874231170659.

[13] A. Millo F, Piano A, Peiretti Paradisi B, Segatori C, et al. Ducted fuel injection: a numerical soot-targeted duct geometry optimization SAE Int J Engines 2022;15(2):297–317. https://doi.org/10.4271/03-15-02-0014.

[14] Millo F, Segatori C, Piano A, Paradisi BPeiretti, et al. An engine parameters sensitivity analysis on ducted fuel injection in constant-volume vessel using numerical modeling. SAE Technical Paper 2021-24-0015; 2021. https://doi.org/10.4271/2021-24-0015.

[15] Li F, Zou R, Xie P. Analysis on spray behavior of ducted fuel injection under different ambient pressures. Int J Multiph Flow 2024;177:104870. https://doi.org/10.1016/j.ijmultiphaseflow.2024.104870.

[16] Godbold C, Gupta I, Kurtz E, Mueller CJ, et al. Experimental investigation of mixing phenomena for ducted fuel injection. Proc Combust Inst 2024;40(1–4):105385. https://doi.org/10.1016/j.proci.2024.105385.

[17] Svensson K, Kim C, Seiler P, Martin G, et al. Performance and emission results from a heavy-duty diesel engine with ducted fuel injection. SAE Technical Paper 2021-01-0503; 2021. https://doi.org/10.4271/2021-01-0503.

[18] K. Svensson, R. Fitzgerald, and G. Martin, "Ducted fuel injection: confirmed re-entrainment hypothesis," SAE Technical Paper 2024-01-2885, 2024, doi:10.4271/2024-01-2885.

[19] Piano A, Segatori C, Millo F, Pesce F, et al. Investigation of ducted fuel injection implementation in a retrofitted light-duty diesel engine through numerical

simulation. SAE Int J Engines 2023;16(5):643–61. https://doi.org/10.4271/03-16-05-0038.
[20] Pastor JV, Micó C, Lewiski F, Bin-Khalid U. Evaluation of the ducted fuel injection concept for medium duty engines and multi-hole nozzles: an optical analysis. Appl Energy 2024;376:124305. https://doi.org/10.1016/j.apenergy.2024.124305.
[21] Nilsen C, Biles D, Mueller CJ. Using ducted fuel injection to attenuate soot formation in a mixing-controlled compression ignition engine. SAE Int J Engines 2019;12(3):309–22. https://doi.org/10.4271/03-12-03-0021.
[22] Nilsen C, Biles D, Yraguen B, Mueller CJ. Ducted fuel injection versus conventional diesel combustion: an operating-parameter sensitivity study conducted in an optical engine with a four-orifice fuel injector. SAE Int J Engines 2020;13(3):345–62. https://doi.org/10.4271/03-13-03-0023.
[23] Nilsen C, Biles D, Yraguen B, Mueller CJ. Ducted fuel injection vs. Conventional diesel combustion: extending the load range in an optical engine with a four-orifice fuel injector. SAE Int J Engines 2021;14(1):47–58. https://doi.org/10.4271/03-14-01-0004.
[24] Mueller CJ, Nilsen CW, Biles DE, Yraguen BF. Effects of fuel oxygenation and ducted fuel injection on the performance of a mixing-controlled compression-ignition optical engine with a two-orifice fuel injector. Appl Energy Combust Sci 2021;6:100024. https://doi.org/10.1016/j.jaecs.2021.100024.
[25] Nilsen CW, Biles DE, Wilmer BM, Mueller CJ. Investigating the effects of duct length and diameter and fuel-injector orifice diameter in a compression-ignition engine equipped with ducted fuel injection. Appl Energy Combust Sci 2021;7:100030. https://doi.org/10.1016/j.jaecs.2021.100030.
[26] Wilmer BM, Nilsen CW, Biles DE, Mueller CJ, et al. Solid particulate mass and number from ducted fuel injection in an optically accessible diesel engine in skip-fired operation. Int J Engine Res 2022;23(7):1226–36. https://doi.org/10.1177/14680874211010560.
[27] Nyrenstedt G, Nilsen CW, Biles DE, Mueller CJ. Ducted fuel injection with Low-net-carbon fuels as a solution for meeting future emissions regulations. Fuel 2023;338:127167. https://doi.org/10.1016/j.fuel.2022.127167.
[28] Şener R, Nilsen CW, Biles DE, Mueller CJ. A computational investigation of engine heat transfer with ducted fuel injection. Int J Engine Res 2023;24(8):3328–41. https://doi.org/10.1177/14680874221149321.
[29] Buurman N, Nyrenstedt G, Mueller CJ. Ducted fuel injection provides consistently lower soot emissions in sweep to full-load conditions. SAE Int J Engines 2024;17(1):3–16. https://doi.org/10.4271/03-17-01-0001.
[30] Yraguen BF, Steinberg AM, Nilsen CW, Wengrove DE, et al. Parametric evaluation of ducted fuel injection in an optically accessible mixing-controlled compression-ignition engine with two- and four-duct assemblies. Int J Engine Res 2024;25(2):245–61. https://doi.org/10.1177/14680874231170653.
[31] Liu X, Im HG, Mueller CJ, Nyrenstedt G. A computational parametric study of ducted fuel injection implementation in a heavy-duty diesel engine. Fuel 2024;358:130228. https://doi.org/10.1016/j.fuel.2023.130228.
[32] Şener R, Nyrenstedt G, Baumgard KJ, Mueller CJ. Determining tolerance requirements for spray-duct alignment in ducted fuel injection. Int J Engine Res 2024. https://doi.org/10.1177/14680874241272820.
[33] Richards KJ, Senecal PK, Pomraning E. CONVERGE 3.1 manual. Madison: Converg Sci 2023.
[34] Millo F, Piano A, Peiretti Paradisi B, Marzano MR, et al. Development and assessment of an integrated 1D-3D CFD codes coupling methodology for diesel engine combustion simulation and optimization. Energies 2020;13(7):1612. https://doi.org/10.3390/en13071612.
[35] Engine combustion Network (ECN) https://ecn.sandia.gov/ Accessed: Dec. 06 2024.
[36] F.R. Westlye, M. Battistoni, S.A. Skeen, J. Manin et al., "Penetration and combustion characterization of cavitating and non-cavitating fuel injectors under diesel engine conditions," SAE Technical Paper 2016-01-0860, 2016. doi:10.4271/2016-01-0860.
[37] Launder BE, Sharma BI. Application of the energy-dissipation model of turbulence to the calculation of flow near a spinning disc. Lett Heat Mass Transf 1974;1(2):131–7. https://doi.org/10.1016/0094-4548(74)90150-7.
[38] Pope SB. An explanation of the turbulent round-jet/plane-jet anomaly. AIAA J 1978;16(3):279–81. https://doi.org/10.2514/3.7521.
[39] Reitz R, Diwakar R. Structure of high-pressure fuel sprays. SAE Technical Paper 870598; 1987. https://doi.org/10.4271/870598.
[40] Amsden AA, O'Rourke PJ, Butler TD. KIVA-II: a computer program for chemically reactive flows with sprays. Los Alamos, NM (United States); 1989. https://doi.org/10.2172/6228444.
[41] Lin SP, Lian ZW. Mechanisms of the breakup of liquid jets. AIAA J 1990;28(1):120–6. https://doi.org/10.2514/3.10361.
[42] Liu A, Mather D, Reitz R. Modeling the effects of drop drag and breakup on fuel sprays. SAE Technical Paper 930072; 1993. https://doi.org/10.4271/930072.
[43] Schmidt DP, Rutland CJ. A new droplet collision algorithm. J Comput Phys 2000;164(1):62–80. https://doi.org/10.1006/jcph.2000.6568.
[44] Maes N, Skeen S, Bardi M, Fitzgerald R, et al. Spray penetration, combustion, and soot formation characteristics of the ECN Spray C and Spray D injectors in multiple combustion facilities. Appl Therm Eng 2020;172:115136. https://doi.org/10.1016/j.applthermaleng.2020.115136.
[45] Westlye, F., Battistoni, M., Skeen, S., Manin, J. et al., "Penetration and combustion characterization of cavitating and non-cavitating fuel injectors under diesel engine conditions," SAE Technical Paper 2016-01-0860, 2016, https://doi.org/10.4271/2016-01-0860.
[46] Amsden AA. KIVA-3V: a block-structured kiva program for engines with vertical or canted valves. NM: Los Alamos; 1997. https://doi.org/10.2172/505339.
[47] Zeuch T, Moréac G, Ahmed SS, Mauss F. A comprehensive skeletal mechanism for the oxidation of n-heptane generated by chemistry-guided reduction. Combust Flame 2008;155(4):651–74. https://doi.org/10.1016/j.combustflame.2008.05.007.
[48] Kazakov A, Frenklach M. Dynamic modeling of soot particle coagulation and aggregation: implementation with the method of moments and application to high-pressure laminar premixed flames. Combust Flame 1998;114(3–4):484–501. https://doi.org/10.1016/S0010-2180(97)00322-2. Aug.
[49] Heywood JB. Internal combustion engine fundamentals. New York : McGraw-Hill Book Company; 1998.
[50] Naber J, Reitz R. Modeling engine spray/wall impingement. SAE Technical Paper 880107; 1988. https://doi.org/10.4271/880107.
[51] Daurer G, Schwarz S, Demuth M, Gaber C, et al. Experimental and numerical analysis of industrial-type low-swirl combustion of hydrogen enriched natural gas including OH* chemiluminescence imaging. Int J Hydrog Energy 2024;80:890–906. https://doi.org/10.1016/j.ijhydene.2024.07.119.
[52] Tonti Federica, Perovšek Jaka, Usandivaras Jose' Zapata, Karl Sebastian, et al. Obtaining pseudo-OH* radiation images from CFD solutions of transcritical flames. Combust Flame 2021;233:111614. https://doi.org/10.1016/j.combustflame.2021.111614.
[53] Hessel R, Yue Z, Reitz R, Musculus M, et al. Guidelines for interpreting soot luminosity imaging. SAE Int J Engines 2017;10(3):1174–92. https://doi.org/10.4271/2017-01-0716.
[54] Modest MF. Radiative heat transfer. Elsevier; 2013. https://doi.org/10.1016/C2010-0-65874-3.
[55] Piano A, Roggio S, Millo F, Garcia A, et al. Numerical and optical soot characterization through 2-color pyrometry technique for an innovative diesel piston bowl design. Fuel 2023;333:126347. https://doi.org/10.1016/j.fuel.2022.126347.
[56] Baker HDean, Ryder EA, Baker NH. Temperature measurement in engineering, 2. Stamford: Omega Press; 1961.